Journal of Materials Chemistry A

Accepted Manuscript

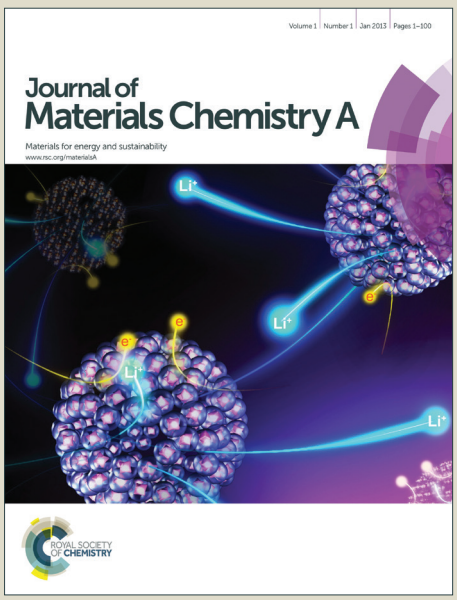

ROYAL SOCIETY OF CHEMISTRY

www.rsc.org/materialsA

Journal Name

RSCPublishing

ARTICLE

Influence of carbon pore size on the discharge capacity of Li-O_2 batteries

Cite this: DOI: 10.1039/x0xx00000x

Ning Ding,[a] Sheau Wei Chien,[a] T. S. Andy Hor,[*ab] Regina Lum,[a] Yun Zong,[a] Zhaolin Liu[*a]

Received 00th January 2012,
Accepted 00th January 2012

DOI: 10.1039/x0xx00000x

www.rsc.org/

Porous carbon materials play a key role in rechargeable Li-O_2 batteries as the oxygen diffusion media and the site for reversible electrode reactions. Despite the tremendous efforts in the synthesis of various porous carbon materials, the influence of carbon materials on cell capacity remains unclear. Based on our study of eight different carbon electrode materials with various pore size and pore volume in Li-O_2 batteries, we found that the initial discharge capacity was hardly affected by the surface area or pore volume. Instead, it was directly correlated with the pore sizes. To further verify this finding, meso- and macro-porous carbon materials with pore size in the range of 20 to 100 nm were prepared using spherical silica as template. The results clearly showed that the cell capacity increases with the increase of pore size and eventually reached its maximum at 7,169 mAh g^{-1} at a pore size of 80 nm. A physical model proposed to illustrate the influence of carbon pore size on cell capacity is the formation of a monolayer of Li_2O_2 with a thickness of 7.8 nm inside the carbon pores during the discharge process which limits the diffusion of incoming oxygen at smaller pore size (< 80 nm).

1 Introduction

Li-air batteries have attracted much attention in recent years due to their high energy density, low-cost and environmental amenity.[1] Ideally, Li-air batteries use oxygen directly from air as an active material at the cathode, and deliver a theoretical energy density of around 3,500 Wh kg^{-1} which is 10 times as high as that of traditional Li-ion batteries.[2,3] With lithium as anode, the cathode of a lithium-air battery is mainly oxygen catalysts loaded porous carbon materials which enables both Li_2O_2 deposition (oxygen reduction) and its decomposition (oxygen evolution) reactions in discharge and charge processes, respectively.[4] Apart from the storage of Li_2O_2, the carbon material is anticipated to provide an effective conductive matrix for electron transfer during these electrode reactions. It is thus crucial to construct a highly-efficient and reliable host carbon structure for Li-air batteries.

Carbon materials with different nanostructures have been developed and used as air cathode in Li-air batteries.[5-14] In general, the capacity of Li-air batteries may be affected by the properties of carbon, e.g. morphology, surface area, porous structure and conductivity.[15,16] Piana et al. chose ether-based electrolytes to investigate seven different types of carbon black, and proposed a direct proportionality between carbon surface area and initial discharge capacity.[17] Such correlation was interpreted as the result of the formation of a Li_2O_2 passivation film on the carbon surface, which was supported by Byon et al. via in-situ monitoring of the Li-O_2 electrochemical deposition on highly oriented pyrolytic graphite (HOPG) using an electrochemical atomic force microscope (EC-AFM).[18] However, formation of Li_2O_2 toroids was more frequently observed in later studies.[19-28] Shao-Horn[29] and Nazar[30] separately unified the two observations with the mechanism of the discharge current amplitude dependent Li_2O_2 morphologies. Under low discharge current the discharge product tends to epitaxially grow on Li_2O_2 surface and form large Li_2O_2 discs or toroids (25-200 nm); whereas high discharge current leads to the formation of small Li_2O_2 nanoparticles (5-15 nm) on the carbon which may eventually form a thin film of Li_2O_2.

The morphology of Li_2O_2 deposited on carbon would significantly affect the specific capacity of the cathode. Conventionally, the applied current on Li-air battery is below 100 mA per gram carbon (mA g_c^{-1}), at which Li_2O_2 discs/toroids tend to form as the dominant product. In this case, the factors that affect the cell capacity are no longer the same as those in the case of the formation of Li_2O_2 thin film. Im et al. reported that the specific capacity was determined by the pore volume of carbon rather than its surface area[31] and larger pore volume that could accommodate more Li_2O_2 was preferable. Researchers from Toyota drew a similar conclusion, with additional claim that mesopore was superior to micropore to yield a higher capacity.[32] However, these results are insufficient due to the lack of consideration of the differences in carbon origin, morphology, surface area, particle size and electrolyte wettability, which all could have an impact on the capacity and cycling behavior of lithium-air cathodes.

Besides the capacity, a critical challenge that limits the practical use of the Li-air batteries is the low coulombic efficiency and low round-trip efficiency, arising from the sluggish reaction kinetics of oxygen reduction reaction (ORR) (during discharge) and oxygen evolution reaction (OER) (during charge) in aprotic electrolytes. In order to improve the efficiency of Li-air batteries, tremendous efforts have been devoted to explore ORR/OER catalysts of different

compositions, such as nitrogen-doped carbon,[33-37] transition metal oxides,[22,38-41] and noble metals.[42-44] In comparison with ORR catalysts, OER catalysts are more critical. This is because the apparent overpotential in charge (0.8-1.2 V) is generally much higher than that in discharge (0.2-0.3 V). Due to the high charge overpotential, the working potential of Li-air batteries is usually above 4.2 V (vs. Li^+/Li). At such high voltage transition metal oxides are superior in electrochemical stability to doped carbons and noble metals.[32] Additionally, for Li-air battery applications, the most practical way is to incorporate ORR/OER catalysts into the carbon matrix to enable synergistic chemical coupling between metal oxide and carbon, leading to possibly further improved catalytic activity.[45] RuO_2 was originally known as an effective OER catalyst in alcohol/CO oxidation and water splitting.[46,47] Recent studies showed that RuO_2,[48,49] hydrated RuO_2[50] and $Pb_2Ru_2O_{7-\delta}$[22] are effective OER catalysts in Li-air batteries. With their presence a coulombic efficiency of ~100% and a round-trip efficiency of 60% to 80% are achievable.[51]

In order to give a more holistic view on the correlation between carbon properties and cell capacity, in the present study we first compared the electrochemical behavior of commercial carbon black (Ketjen black, acetylene black and Super P), multi-walled carbon nanotubes (MWCNT) and ordered mesoporous carbon (OMC), and other commonly used inverse opal carbon (IOC), activated carbon and reduced graphene oxide (rGO). Subsequently, we fabricated meso- and macro- porous carbons using phenol formaldehyde resin as precursor and silica nanospheres of selected particle sizes as templates, to investigate the influence of the pore size in the porous carbon on the electrochemical performance of rechargeable Li-O_2 batteries.

2 Experimental

2.1 Sources of eight carbon materials

MWCNT (multi-wall carbon nanotube, OD: <8 nm, length: 10-30 μm) and OMC (ordered mesoporous carbon) were purchased from Nanjing XFNANO Materials Tech Co., Ltd. Three types of carbon blacks, acetylene black (from MTI Corp.), Super P and Ketjen black (EC-330J), were used in this study. Activated carbon was prepared following a reported method.[52] Inverse opal carbon (IOC) was synthesized using assembled silica nanospheres as template.[53] Briefly, furfural and resorcinol were infiltrated into dried silica template (ST-OL, Nissan Chemical Industries, Ltd.), followed by a carbonization process at 1400 °C over 2 h. The silica template was then removed by HF (46%) at room temperature over 12 h. Graphene oxide was prepared via a modified Hummers method,[54] and purified via a dialysis process over 1 week and freeze-dried. The reduction reaction was carried out at 1000 °C under 5% H_2/Ar atmosphere for 1 h. The reduced product, reduced graphene oxide (rGO), was harvested as loosely packed powder with a dark color and used in Li-O_2 battery test.

2.2 Synthesis of meso/macro-porous carbon materials (PC)

Phenol formaldehyde (PF) resin was chosen as the carbon precursor and silica colloidal particles (Nissan Chemical Industries, Ltd.) with different particle sizes were used as template to prepare the meso/macro- porous carbon. The sample preparation process was as follows: 1) Phenol (20 g) was dissolved into of formaldehyde (37-40%) (64 ml), with of ammonia solution (28% NH_3 in H_2O) (4 ml) added as a catalyst. The solution mixture was heated to 80 °C to enable a fast polymerization reaction which completes within 1 h. The resultant resin was precipitated by adding ice water (80 ml) and retrieved via centrifugation, and washed with deionized water for three times. Finally the resin was re-dissolved in acetone as a stock solution with a concentration of around 0.5 g mL^{-1}; 2) Silica colloidal solution was dried at 100 °C for 3 days to form the silica template. Silica template (5 g) was then mixed with PF resin solution (1.1 ml) and acetone (5 ml). The mixture was sonicated for 15 min to get PF resin infiltrated into the silica voids. After vacuum drying, the PF resin/silica composite was carbonized at 900 °C under Ar atmosphere for 3 h; 3) After carbonization, the silica template was removed repeatedly by reacting with 4 M NaOH (80 ml) at 80 °C for 2 h. The retrieved porous carbon was rinsed with deionized water (40 ml) for 3 times and subsequently dried at 120 °C for 12 h for battery test. The samples obtained were denoted by PC20, PC40, PC60, PC80 and PC100, where PC stands for porous carbon and the numbers represent the pore size in nm as observed under microscope. The sample prepared via direct carbonization of PF resin was denoted as PC00.

2.3 Characterization

Powder X-ray diffraction (XRD) analysis was carried out on a Bruker D8 X-ray diffractometer with a Cu-Kα radiation (λ=1.54 Å). Transmission electron microscope (TEM) images were taken on a Philips CM300 FEGTEM with an accelerating voltage of 200 kV. Surface area of carbon materials was measured using the Brunauer-Emmett-Teller (BET) method from nitrogen gas adsorption–desorption isotherms at 77 K (ASAP 2020, Micromeritics).

2.4 Electrochemical measurement

The ORR and OER performances were evaluated using an electrochemical workstation (Metrohm, Autolab). The working electrode was a glassy carbon rotating disk electrode with a disk diameter of 5 mm (Autolab) with a Pt foil as the counter electrode and saturated Ag/AgCl as the reference electrode. 5 mg of carbon was dispersed in 0.8 ml of ethanol and 0.2 ml of Nafion® 117 solution (~5 wt.%, Sigma-Aldrich) under sonication. Then 10 μL of the suspension was pipetted onto the disk and dried in air. ORR and OER measurements were carried out in 0.1 M KOH at a rotating speed of 1,600 rpm between -0.8 V and 1.0 V.

To prepare the cathode for a Li-O_2 battery, the carbon sample was mixed with polyvinylidene fluoride (PVDF, Kynar 761) binder in N-methyl-2-pyrrolidone (NMP, Sigma-Aldrich) in a weight ratio of 7:3 to form a black slurry. The slurry was then coated evenly onto a piece of stainless steel (SS) gauze with a diameter of 15 mm (200 mesh woven from wires of 0.05 mm in diameter, type 316). The electrode was dried in oven at 120 °C over 5 h and then transferred into an Ar-filled glove box (H_2O < 0.1 ppm, O_2 < 0.1 ppm). The mass loading of carbon is 1.0±0.1 mg. Electrochemical performance

of Li-O_2 batteries was carried out using CR2032 coin-type cells with 19 holes (diameter: ~1 mm) on the positive shell as oxygen diffusion paths. The cells were assembled in the glove box with the as-prepared cathode, metallic lithium foil (diameter: 13 mm) as counter electrode, the glass fiber separator (diameter: 16 mm, Whatman®, GF/B) as separator and 1 M lithium trifluoromethanesulfonyl (LiTFS, 99.995%, Sigma-Aldrich) dissolved in triethylene glycol dimethyl ether (TEGDME, 99%, Sigma-Aldrich) as electrolyte in an Ar-filled glove box (Labmaster200, Mbraun, Germany). The coin cell was sealed into a reagent bottle with a volume of 1 L and then purged with oxygen (99.9995%) at a gas flow of 500 ml min^{-1} for 20 min. The cell was tested in an airtight condition and the calculated pressure fluctuation in the reagent bottle during charge-discharge test was less than 0.5% (based on 1.1 mg carbon loading and the capacity of 10,000 mAh g^{-1}) which is negligible. In order to minimize the impact of the trace amount of moisture, 50 ml drying pearls orange (Sigma-Aldrich) was placed at the bottom of the reagent bottle. The overall Li-air battery system is schematically shown in Fig. S1†. Charge-discharge experiments were performed at a constant current of 0.05 mA (50 mA g_c^{-1}, for eight different carbon materials) and 0.1 mA (100 mA g_c^{-1}, for PC carbon) between 2.0 and 4.3 V on battery testers (NEWARE BTS-610, China) at room temperature.

3 Results and discussion

3.1 Influence of various carbon materials on cell capacity

Fig. 1 shows the initial charge-discharge voltage profiles of Li-air batteries with different carbon materials as air electrodes. It can be seen that MWCNT delivers the lowest capacity of only 1,300 mAh g^{-1}, while rGO gives the highest capacity of above 8,000 mAh g^{-1}. The discharge capacities of three types of carbon black (Ketjen black, acetylene black and Super P) electrodes are 2,865, 3,512 and 3,399 mAh g^{-1}, respectively. The discharge capacities of the mesoporous carbon materials (OMC and IOC) greatly differ from each other. IOC delivers a capacity of 4,503 mAh g^{-1}, which is two times as high as that of OMC. Such capacity diversity can be attributed to the different properties of carbon materials.

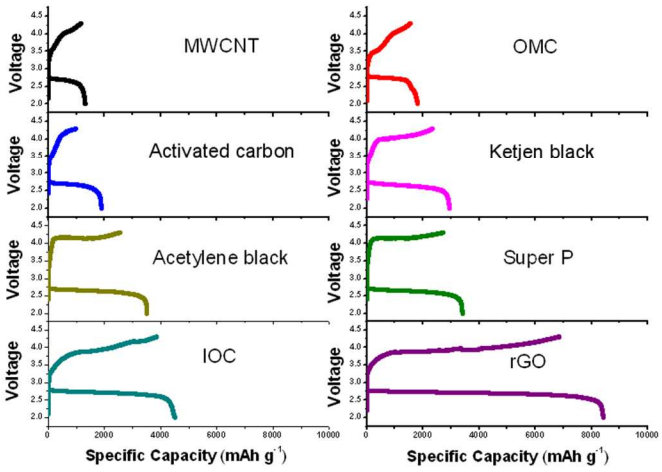

Fig. 1 Initial charge-discharge voltage profiles of Li-O_2 batteries with various carbons cycled at a constant current of 0.05 mA (50 mA g_c^{-1}).

Table 1 Surface area and pore characteristics of various carbons and their influence on the capacity of Li-O_2 batteries.

Carbon Materials	Surface Area (m^2 g^{-1})	Pore Volume (cm^3 g^{-1})	Pore Size (nm)	Discharge Capacity (mAh g^{-1})
MWCNT	929	1.64	7.0	1,311
OMC	863	1.14	5.2	1,812
Activated carbon	1,230	1.07	4.7	1,897
Ketjen black	818	1.17	7.7	2,865
Super P	62	0.32	11.9	3,399
Acetylene black	56	0.16	11.4	3,512
IOC	794	3.17	16.0	4,504
rGO	361	1.58	17.5	8,418

Previous studies suggested a correlation between the capacity and the surface area or the porous structure of carbon. However, very limited carbon sources investigated in these studies imposed high likelihood of inaccuracy.[31,55] In addition, the used carbonate electrolytes[32,56-58] are vulnerable to the attack of superoxides, causing degradation of electrolyte and formation of Li_2CO_3 which could also affect the conclusion.[59-61] To reveal a more reliable and conclusive correlation, a larger number of carbon materials are needed to be used together with a more stable electrolyte. In our study the electrolyte was triethylene glycol dimethyl ether (TEGDME). Despite the dispute over its long-term stability,[62-64] Li_2O_2 was found to be the only discharge product in TEGDME as confirmed by XRD as shown in Fig. S2†.

In order to elucidate the correlation of cell capacity with the properties of the carbon matrix, in Table 1 we summarized the surface area, pore size and pore volume of the above-mentioned eight different carbon materials which were obtained from N_2 adsorption-desorption isotherms. One can see that the activated carbon exhibits the highest surface area of 1,230 m^2 g^{-1}, while acetylene black gives the smallest surface area of 56 m^2 g^{-1}. Interestingly, with a surface area of as low as 5% of that of the activated carbon, the acetylene black delivers 2 times of the discharge capacity, which clearly contradicts the previous findings.[17] Other incompliant examples are Ketjen black and IOC that possess similar surface area while the latter delivers 57% more capacity; or from acetylene black to rGO to IOC where the surface area continuously increases but no unidirectional changes in the capacity were seen. Similar incompliance is seen on the correlation between cell discharge capacity and the pore volume. As the pore volume gradually increases from 0.16 to 1.14 cm^3 g^{-1} (Acetylene Black→Super P→Active Carbon→OMC), a steady decrease in the cell discharge capacity is observed, which contradicts the previous findings.[31] From 1.14 to 3.17 cm^3 g^{-1} the changes in the cell discharge capacity is rather complicated than any unidirectional trend. Obviously, the simple proportionality of cell discharge capacity to either the surface area or pore volume of carbon does not comply in these cases.

If we assume that the difference in the microstructure of the carbon materials plays a role here, the above-described 8 different carbon materials can be divided into four types: Type I are carbon blacks, including acetylene black, Super P and Ketjen black that are small carbon granules obtained from thermal decomposition of organic compounds. The difference is that the average particle size of

acetylene black and Super P is around 40 nm, whereas Ketjen black are much smaller carbon granules with a much larger surface area. Type II are mesoporous carbons, including OMC, IOC and activated carbon. The OMC and IOC are prepared from silica templates and thus possess well-ordered mesopores, whereas the activated carbon in this work was prepared using rice hull as precursor (followed by hydrofluoric acid and steam activation) and possesses mesoporous structure with larger pore size (compared to the conventional activated carbon) due to the presence of silica particles in cell wall. Type III carbon is represented by MWCNT that possesses a tunnel structure, with the diameter of tunnel being smaller than 8 nm. Type IV carbon is a 3D rGO network that comprises mono- and multi-layer rGO flakes, made from oxidation exfoliation of graphite by chemical method followed by high temperature reduction using H_2/Ar. The 4 types of carbon materials are schematically shown below in Fig. 2.

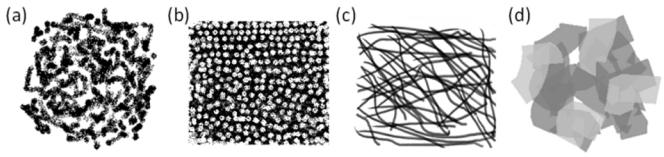

Fig. 2 Schematic drawings of four types of microstructures for: (a) Carbon blacks, i.e. acetylene black, Super P and Ketjen black. (b) Mesoporous carbons, i.e. OMC, IOC and activated carbon. (c) MWCNT and (d) rGO.

One can see that even if comparisons are made within the same type of carbons, the correlation between the discharge capacity and the surface area or the pore volume of carbon materials are still invalid, e.g. for surface area effect, in Type I carbon materials the Ketjen black possesses the highest surface area (818 m^2 g^{-1}, ~13 times as high as that of Super P and acetylene black), but delivers the lowest capacity; and in Type II carbon materials OMC and IOC possess similar surface area of around 800 m^2 g^{-1}, however, the capacity of IOC is about 2.5 times as high as that of OMC. For the pore volume effect, in Type I carbon materials it seems that the cell discharge capacity decreases with the increases of pore volume, while the inverse trend is seen in the Type II carbon materials. Such random correlation between the cell capacity and the surface area and the non-unidirectional correlation between the cell capacity and the pore volume (dependent on the type/microstructure of the carbon materials) imply that there could be a 3rd factor in the microstructure that plays a more critical role in the amplitude of the cell discharge capacity.

Interestingly, if we look carefully at the changes of pore size as the cell discharge capacity increases in Table I, a much better correlation can be observed. To a large extent, the cell discharge capacity exhibits proportionality to the pore sizes. With some fluctuation the cell capacity rises from 1,897 mAh g^{-1} to 8,418 mAh g^{-1}, as the pore size increases from 4.7 nm (for activated carbon) to 17.5 nm (for rGO). A distinct exception here is the MWCNT which only delivers a capacity of 1,311 mAh g^{-1}, though a medium pore size of 7.0 nm was measured. This abnormality might be attributed to the large length-to-diameter ratio of MWCNT which can be as high as 3,750:1. The ultra-long MWCNT is not in favor of oxygen diffusion inside the tubes, and its open ends can be easily blocked by the deposition of Li_2O_2. Such blockage results in low utilization of pore volume inside of MWCNT, and Li_2O_2 mainly precipitates outside of tubes.[25,29] The deduced correlation between carbon pore volume and discharge capacity[31] in fact can be traced to the variation in the pore size. As both the pore volume and surface area varied in the above 8 different carbon materials, it is so far insufficient to draw the conclusion that the pore size is the key determining factor to the cell discharge capacity. New experiments are devised below to eliminate the significant difference in carbon microstructure (including surface area and pore volume) and verify the pore size effect.

3.2 Influence of carbon pore size on cell capacity

Carbon materials prepared from different precursors at different carbonization temperatures may display varied conductivity and electrolyte wettability, and thus introduce unnecessary complications to the study. Hence, we carefully designed and synthesized a series of meso- and macro-porous carbons using PF resin as carbon precursor and silica spheres with different sizes as templates. The pore size of carbon increases from 20 nm for PC20 to 100 nm for PC100, as shown in their TEM images (Fig. 3). For PC00 that was prepared in the absence of silica template, no clear carbon pore is visible. Nevertheless, BET analysis reveals pores of 2.4 nm in PC00. The pore size and BET surface area of all the resultant porous carbon materials are summarized in Table 2. Except for PC00, all the carbon materials possess similar surface areas of around 850 m^2 g^{-1}. As the ratio of silica and carbon precursor (5 g silica template and 1.1 PF resin solution) was fixed in the synthesis, the five resultant porous carbon materials (PC20 to PC100) should also possess similar cumulative volume of pores (assuming all silica spheres have been covered by carbon precursor, 2.4 ~ 3.3 cm^3 g^{-1} based on BET results).

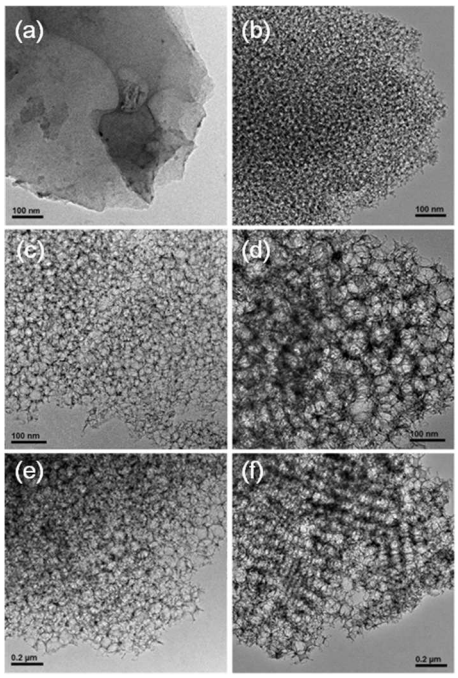

Fig. 3 TEM images of the synthesized meso- and macro-porous carbons: (a) PC00, (b) PC20, (c) PC40, (d) PC60, (e) PC80 and (f) PC100.

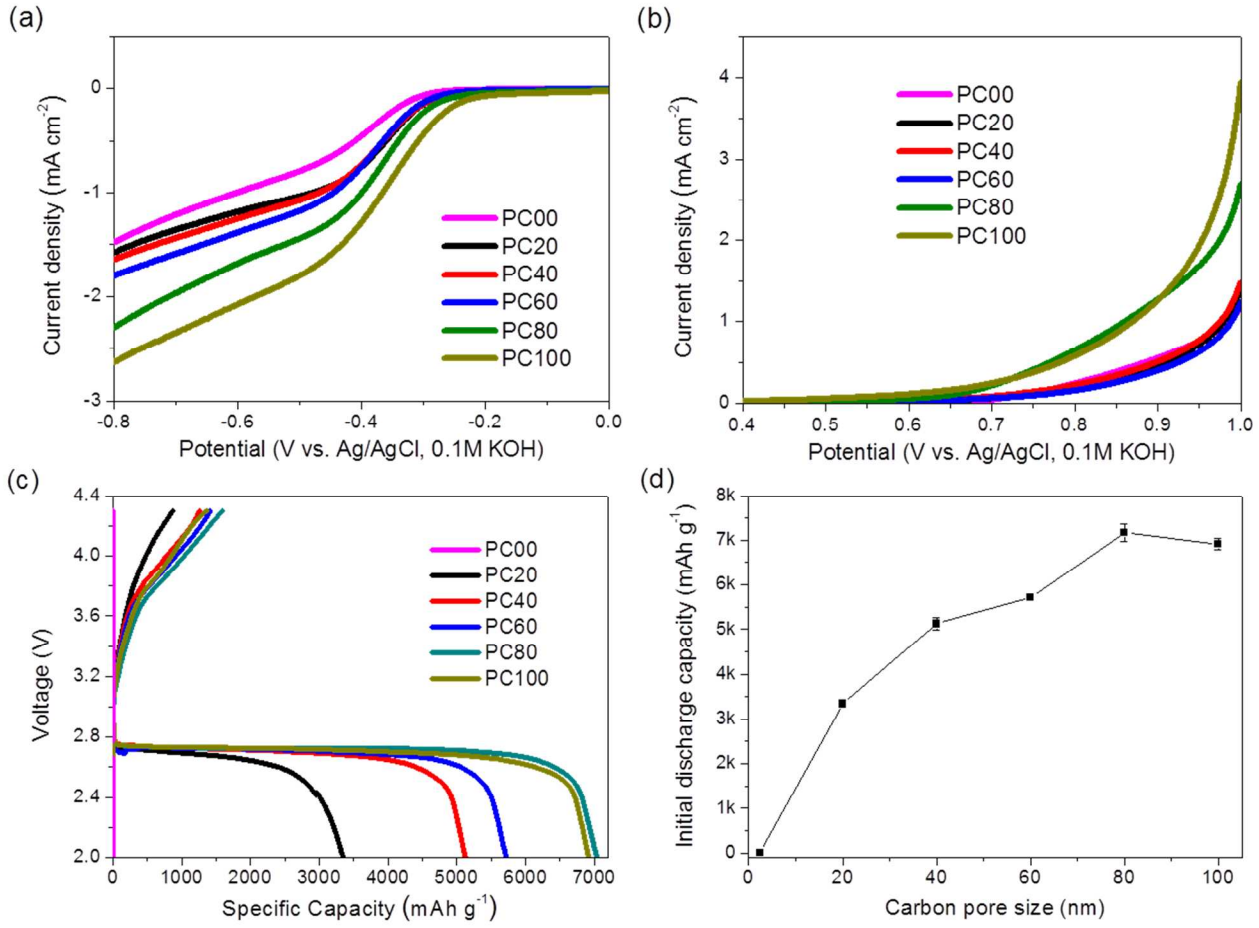

Fig. 4 Electrochemical performance of the synthesized meso- and macro-porous carbons: Polarization curves of (a) ORR and (b) OER activities in 0.1 M KOH alkali solution. (c) Initial charge-discharge voltage profiles tested in Li-O_2 batteries cycled at a constant current of 0.1 mA (100 mA g_c^{-1}). (d) The correlation between carbon pore size and cell capacity (all data have been repeated for 3 times).

Table 2 Surface area and pore characteristics of the synthesized meso- and macro-porous carbons with different types of silica as templates.

Sample name	Type of silica template (Snowtex®)	BET surface area ($m^2 g^{-1}$)	Pore volume ($cm^3 g^{-1}$)	Carbon pore size from TEM images (nm)
PF00	N.A.	256	0.15	2.4*
PF20	ST-50	883	2.72	20
PF40	ST-XL	879	3.27	40
PF60	ST-YL	817	2.82	60
PF80	ST-ZL	859	2.48	80
PF100	MP-1040	823	2.38	100

* Pore size value is derived from BET analysis.

The ORR and OER properties of porous carbons were evaluated using rotating disk electrode (RDE) method, and the results are shown in Fig. 4a and b. In ORR process (Fig. 4a), the oxygen reduction current density (at -0.8 V) seems proportional to the carbon pore size, e.g. 1.48 mA cm^{-2} for PC00, 1.64 mA cm^{-2} for PC40 and 2.30 mA cm^{-2} for PC80, respectively. In OER process (Fig. 4b), the carbon materials with pore sizes up to 60 nm almost show no difference in OER currents. However, a higher OER current density was observed as the pore size was increased to 80 nm. At the pore size of 100 nm (PC100), its OER current density at 1.0 V vs. Ag/AgCl is almost two times as high as that of the carbons with pore sizes below 60 nm. This clearly shows that larger carbon pore size is in favour of both ORR and OER processes, which is due to the improved oxygen diffusion. It should be noted that the RDE data was collected in alkaline aqueous solution, whereas the cell in our Li-air system was cycled in aprotic electrolyte. To obtain more relevant results, the charge and discharge voltage profiles of Li-air batteries using these PC samples as cathodes are recorded and shown in Fig. 4c. In contrary to the RDE results, all porous carbons exhibit a discharge voltage plateau at around 2.72 V with hardly noticeable difference in the voltage plateaus. The different behaviour shown in RDE experiments and battery performance tests might be attributed to the different rate-limiting process in electrochemical reactions. In alkaline solution, the oxygen solubility is significantly higher and the limiting process is the oxygen diffusion rate in the electrode. Naturally, larger carbon pores are beneficial and thus showing higher

ORR and OER currents. However, in aprotic electrolyte due to its higher viscosity and the much lower oxygen solubility the limiting process becomes the dissolution rate of oxygen into electrolyte,[65] leading to a similar voltage plateau for all porous carbons. Nevertheless, the carbon pore size variation still shows a clear impact on the discharge capacity. With the increase of carbon pore size from 20 nm (for PC20) all the way to 80 nm (PC80), the discharge capacity rises from 3,343 mAh g^{-1} to 7,169 mAh g^{-1} accordingly (Fig. 4d). This is consistent with our studies above on various carbon materials. The slightly smaller discharge capacity at the pore size of 100 nm seems to suggest that at sufficiently large pore size (when the access to the surface inside pores and the blockage of Li_2O_2 are unlikely issues), the surface area could play a role where larger surface area enables a higher capacity. It is worth noting that the optimal pore size of 80 nm may be only suitable for the OMCs derived from PF resin, rather than other types of carbon materials, such as rGO. But we believe that there should be still an optimal pore size for rGO. In fact, rGO via freeze drying,[19] where larger pores can be left, inclines to delivering higher capacity (> 5000 mAh g-1) than that prepared via conventional drying (~2500 mAh g-1).[8,66]

Though a discharge capacity of around 7,000 mAh g^{-1} is achievable by optimizing the carbon pore size, the corresponding charge capacity is as low as 1,600 mAh g^{-1} (Fig. 4c). The charge capacity is little influenced by carbon pore size due to the poor OER activity of pure carbon. Furthermore, the accumulation of undecomposed Li_2O_2 in the following cycle can block the oxygen diffusion path, leading to a fast capacity fading. In principle, the coulombic efficiency can be simply improved by setting a higher cut-off voltage; however, in practice it is limited by the electrochemical stability window of the electrolytes. An appropriate solution is to add an effective OER catalyst that reduces the overcharge potential of Li_2O_2 decomposition. Herein, RuO_2 nanoparticles were introduced into PC100, leading to complete decomposition of Li_2O_2 and a coulombic efficiency of ~100%. As the decoration of RuO_2 also reduces the pore size, the cell capacity decreases with the amount of RuO_2 on the carbon matrix (Fig. S3†.). The capacity variation of RuO_2/PC100 further confirmed the effect of the carbon pore size on the cell capacity of Li-O_2 batteries.

3.3 Mechanism study of pore size effect on cell capacity

If carbon pores are completely filled with Li_2O_2 in Li-O_2 battery tests, cell capacity should reach a constant value of 16,128 mAh g^{-1}, which is much higher than experimental data (line a in Fig.5, see supporting information for calculation details). In order to understand the difference, especially in the case of sufficiently large pore size, we assume that a thin layer of Li_2O_2 formed as discharge product inside the carbon pores. The poor electrical conductivity of the Li_2O_2 layer prevents further discharge, resulting in partial utilization of the pore volume. The thickness of the Li_2O_2 is likely to be decided by the diameter of the primary Li_2O_2 particles of 7.8 nm, as derived from XRD pattern (Fig. S2†) using the Scherrer equation. With the assumption of a thin layer of 7.8 nm of Li_2O_2 inside the carbon pores, one would deduce the correlation as a reduced capacity with the increase of pore size (line b in Fig. 5) which contradicts with our experimental data. To find out the cause of this discrepancy, TEM study was carried out to understand how the discharge product, Li_2O_2, was deposited on the porous carbons. As polymer binder may fill the carbon pore thus affecting the observation on Li_2O_2 deposition, a binder free electrode was carefully devised. In a typical electrode preparation process, PC carbon was dispersed in acetone and the dispersion was dropped onto a Cu TEM grid coated by lacey carbon that is in favor of oxygen diffusion. The mass of carbon loading on Cu TEM grid is typically about 20 μg, which is much higher than the loading in conventional TEM samples. The as-prepared grid electrode was sandwiched between polyethylene separator (Asahi Kasei) at the electrolyte side and stainless steel (SS) gauze at the O_2 side. Whatman® glass fiber (GF/B) was used as separator in cell assembling. A discharge current of 2 μA (100 mA g_c^{-1}) was applied, which was tested to be sufficient to yield the same morphology of Li_2O_2 as the discharged product in the cell with PC100 loaded on SS gauze discussed above. The discharge voltage profiles (vs. depth of discharge, DOD) of PC100 loaded on SS gauze and on Cu grid are shown in Fig. S4†. Both cells show a long voltage plateau at 2.72 V. The almost identical voltage profiles indicate similar discharge reactions which are likely lead to similar morphologies of the generated Li_2O_2 in two cells. The falling voltage slope of PC100 loaded on Cu grid at 2.5 V (DOD: 85%) may be due to the Li_2O_2 precipitation on lacey carbon.

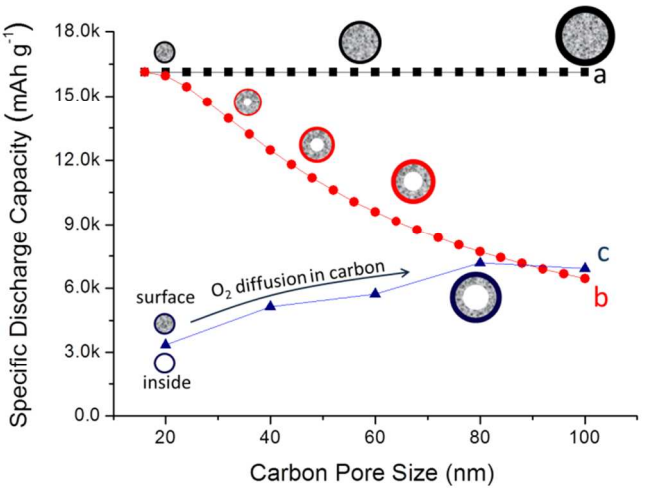

Fig. 5 Physical models of Li_2O_2 stored in porous carbon: line a represents that all carbon pores are fully filled by Li_2O_2; line b is to assume forming a monolayer of Li_2O_2 (with a thickness of 7.8 nm) inside of carbon pores; line c is the experimental data.

TEM images taken from the discharged PC20 and PC100 on Cu grid are shown in Fig. 6. Compared to the pristine samples, a significant increase in image contrast is observed in the discharged samples as the result of the precipitation of Li_2O_2 on porous carbon materials (Fig. S5†.). The presence of Li_2O_2 in the carbon pores is also approved by the electron diffraction patterns (as shown in the inset to Fig. 6b and d). Some distinctly dark areas are seen at the edge of PC20 (marked in Fig. 6a), which may be from the "bulky"

accumulation of Li_2O_2. Such accumulation of Li_2O_2 at the edge of porous carbon may limit or even block the diffusion of oxygen into the pores, thus leading to a low capacity. With large pore size (100 nm) the blockage of pores by the discharged Li_2O_2 became unlikely and the diffusion of oxygen into the carbon pores was significantly improved. Consequently, a homogenous Li_2O_2/PC100 composite was obtained (Fig. 6c). TEM image with higher magnification (Fig. 6d) shows that Li_2O_2 inside PC100 possesses a hollow structure with thickness of Li_2O_2 being ~10 nm, which supports our model b. The capacity of PC80 (7,169 mAh g^{-1}) is slightly lower than the theoretical value of model b, with over 90% utilization rate of carbon pore volume. At the pore size of 100 nm a reduced cell capacity (6,917 mAh g^{-1} for PC100) was seen, which fits the trend of model b. As described previously, at sufficiently large pore size the surface volume starts to play a role. Further increase of pore size will lead to a reduced surface area thus imposes negative impact to the cell discharge capacity. Besides, too large carbon pores may also weak the mechanical property thus cause structure failure of carbon matrix during electrode preparation, leading to loss of electrical contact and fast capacity fading. This hypothesis can be supported by a recent work in which hierarchically porous carbon with honeycomb-like structure was investigated, where the capacity of porous carbon with a pore size of 400 nm (3,233 mAh g^{-1}) was lower than that with a pore size of 100 nm (3,912 mAh g^{-1}) at a current density of 0.05 mA cm^{-2}.[67] It is worth noting that our PC100 exhibits a higher capacity (6,917 mAh g^{-1} at the current density of 0.057 mA cm^{-2}), which may be attributed to the more stable carbon matrix produced from aromatic compound (PF resin) precursors.

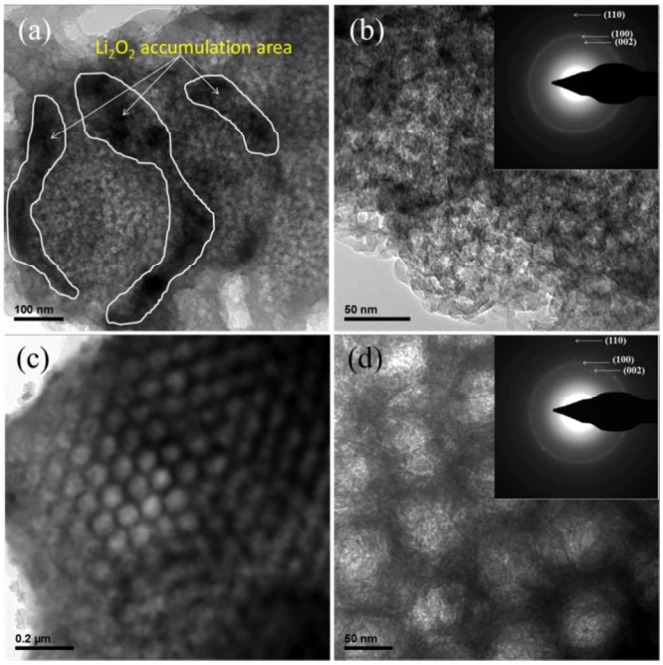

Fig. 6 TEM images of the discharged samples: (a) Low-magnification TEM of PC20. (b) High-magnification TEM of PC20. (c) Low-magnification TEM of PC100. (d) High-magnification TEM of PC100. The cells were discharged to 2 V at a constant current of 2.0 μA. The accumulation areas of Li_2O_2 on PC20 are marked and electron diffraction patterns (the inset) are shown to indicate the presence of Li_2O_2 in the carbon pores.

4 Conclusions

A direct correlation between carbon pore size and cell capacity has been proposed based on the results obtained from the investigation of eight different carbon materials. In general, larger pore size tends to yield higher capacity. The correlation was further confirmed using a series of intentionally designed and synthesized porous carbons with uniform pore sizes in the range from 20 to 100 nm. Electrochemical results showed that at the discharge current of 0.1 mA the cell capacity increases with the pore size and eventually reach its maxima at 7,169 mAh g^{-1} at the pore size of 80 nm. A physical model is proposed to illustrate the influence of carbon pore size on cell capacity, in which a monolayer of Li_2O_2 with a thickness of 7.8 nm forms inside the carbon pores during the discharge process. The cell capacity increases with increasing pore size when the pore size is smaller than 80nm. This is attributed to higher accumulation of Li_2O_2 at the carbon edge for smaller pores, which limits or even blocks the oxygen diffusion into carbon pores, resulting in a low utilization rate of pore volume. An optimal carbon pore size at the discharge current of 0.1 mA is about 90 nm, with a theoretical pore utilization rate of 100%. The cell capacity fades slightly to 6,917 mAh g^{-1} when carbon pore size increased from 80 to 100 nm. This is due to the slightly smaller surface area. This new correlation between carbon pore size and cell capacity is anticipated to facilitate the selection of carbon materials as electrode substrate for high-performance Li-O_2 batteries.

Acknowledgements

This research was supported by the Advanced Energy Storage Research Programme (IMRE/12-2P0503 and IMRE/12-2P0504), Institute of Materials Research and Engineering (IMRE) of the Agency for Science, Technology and Research (A*STAR), Singapore.

Notes and references

[a]*Institute of Materials Research and Engineering, A*STAR (Agency for Science, Technology and Research), 3 Research Link, Singapore 117602, Singapore. E-mail: zl-liu@imre.a-star.edu.sg; Fax:+65-68720785; Tel: +65-68727532*

[b]*Department of Chemistry, National University of Singapore, 3 Science Drive 3, Singapore 117543. E-mail: andyhor@imre.a-star.edu.sg; Fax:+65-68720785; Tel: +65-68744341*

†Electronic Supplementary Information (ESI) available: XRD pattern, additional TEM images and electrochemical data. See DOI: 10.1039/b000000x/

1 B. Dunn, H. Kamath, J.-M. Tarascon, *Science,* 2011, **334,** 928-934.
2 P. G. Bruce, S. A. Freuberger, L. J. Hardwick, J.-M. Tarascon, *Nat. Mater.,* 2012, **11,** 19-29.
3 Y. Wang, G. Z. Cao, *Adv. Mater.* 2008, **20,** 2251-2269.
4 F. Cheng, J. Chen, *Chem. Soc. Rev.,* 2012, **41,** 2172-2192.
5 J.-B. Park, J. Lee, C. S. Yoon, Y.-K. Sun, *ACS Appl. Mater. Interfaces,* 2013, **5,** 13426-13431.
6 Y. F. Li, Z. P. Huang, K. Huang, D. Carnahan, Y. C. Xing, *Energy Environ. Sci.,* 2013, **6,** 3339-3345.

7 J. Park, Y.-S. Jun, W.-R. Lee, J. A. Gerbec, K. A. See, G. D. Stucky, *Chem. Mater.,* 2013, **25,** 3779-3781.
8 Z. Guo, J. Wang, F. Wang, D. Zhou, Y. Xia, Y. Wang, *Adv. Funct. Mater.,* 2013, **23,** 4840-4846.
9 V. Etacheri, D. Sharon, A. Garsuch, M. Afri, A. A. Frimer, D. Aurbach, *J. Mater. Chem. A,* 2013, **1,** 5021-5030.
10 S. Y. Kim, H.-T. Lee, K.-B. Kim, *Phys. Chem. Chem. Phys.,* 2013, **15,** 20262-20271.
11 Y. Chen, F. Li, D.-M. Tang, Z. Jian, C. Liu, D. Golberg, A. Yamada, H. Zhou, *J. Mater. Chem. A,* 2013, **1,** 13076-13081.
12 M. Olivares-Marín, P. Palomino, J. M. Amarilla, E. Enciso, D. Tonti, *J. Mater. Chem. A,* 2013, **1,** 14270-14279.
13 H. W. Park, D. U. Lee, Y. Liu, J. Wu, L. F. Nazar, Z. Chen, *J. Electrochem. Soc.,* 2013, **160,** A2244-A2250.
14 H.-D. Lim, K.-Y. Park, H. Song, E. Y. Jang, H. Gwon, J. Kim, Y. H. Kim, M. D. Lima, R. O. Robles, X. Lepró, R. H. Baughman, K. Kang, *Adv. Mater.,* 2013, **25,** 1348-1352.
15 C. N. Chervin, M. J. Wattendrof, J. W. Long, N. W. Kucko, D. R. Rolison, *J. Electrochem. Soc.,* 2013, **160**, A1510-A1516.
16 S. Liu, Z. Wang, C. Yu, Z. Zhao, X. Fan, Z. Ling, J. Qiu, *J. Mater. Chem. A,* 2013, **1,** 12033-12037.
17 S. Meini, M. Piana, H. Beyer, J. Schwämmlein, H. A. Gasteiger, *J. Electrochem. Soc.*, 2012, **159,** A2135-A2142.
18 R. Wen, M. Hong, H. R. Byon, *J. Am. Chem. Soc.,* 2013, **135,** 10870-10876.
19 Z. L. Wang, D. Xu, J.-J. Xu, L.-L. Zhang, X.-B. Zhang, *Adv. Funct. Mater.,* 2012, **22,** 3699-3705.
20 R. Black, J.-H. Lee, B. Adams, C. A. Mims, L. F. Nazar, *Angew. Chem. Int. Ed.,* 2012, **51,** 1-6.
21 R. Black, S. H. Oh, J.-H. Lee, T. Yim, B. Adams, L. F. Nazar, *J. Am. Chem. Soc.,* 2012, **134,** 2902-2095.
22 S. H. Oh, R. Black, E. Pomerantseva, J.-H. Lee, L. F. Nazar, *Nat. Chem.,* 2012, **4,** 1004-1010.
23 H.-G. Jung, H.-S. Kim, J.-B. Park, I.-H. Oh, J. Hassoun, C. S. Yoon, B. Scrosati, Y.-K. Sun, *Nano Lett.,* 2012, **12**, 4333-4335.
24 J.-B. Park, J. Hassoun, H.-G. Jung, H.-S. Kim, C. S. Yoon, I.-H. Oh, B. Scrosati, Y.-K. Sun, *Nano Lett.,* 2013, **13,** 2971-2975.
25 Z. H. Cui, W. G. Fan, X. X. Guo, *J. Power Sources,* 2013, **235,** 251-255.
26 W. Fan, Z. Cui, X. Guo, *J. Phys. Chem. C,* 2013, **117,** 2623-2627.
27 R. R. Mitchell, B. M. Gallant, C. V. Thompson, Y. Shao-Horn, *Energy Environ. Sci.,* 2011, **4,** 2952-2958.
28 R. R. Mitchell, B. M. Gallant, Y. Shao-Horn, C. V. Thompson, *J. Phys. Chem. Lett.,* 2013, **4,** 1060-1064.
29 B. M. Gallant, D. G. Kwabi, R. R. Mitchell, J. Zhou, C. V. Thompson, Y. Shao-Horn, *Energy Environ, Sci.,* 2013, **6,** 2518-2528.
30 B. D. Adams, C. Radtke, R. Black, M. L. Trudeau, K. Zaghib, L. F. Nazar, *Energy Environ, Sci.,* 2013, **6,** 1772-1778.
31 S. B. Ma, D. J. Lee, V. Roev, D. Im, S. -G. Doo, *J. Power Sources,* 2013, **244,** 494-498.
32 M. Hayashi, H. Minowa, M. Takahashi, T. Shodai, *Electrochemistry,* 2010, **78,** 325-328.
33 G. Wu, N. H. Mack, W. Gao, S. Ma, R. Zhong, J. Han, J. K. Baldwin, P. Zelenay, *ACS Nano,* 2012, **6,** 9764-9776.
34 P. Kichambare, S. Rodrigues, J. Kumar, *ACS Appl. Mater. Interfaces,* 2012, **4,** 49−52.
35 X. Lin, X. Lu, T. Huang, Z. Liu, A. Yu, *J. Power Sources,* 2013, **242,** 855-859.
36 H. Nie, H. Zhang, Y. Zhang, T. Liu, J. Li, Q. Lai, *Nanoscale,* 2013, **5,** 8484-8487.
37 Y. Li, J. Wang, X. Li, D. Geng, M. N. Banis, R. Li, X. Sun, *Electrochem. Commun.,* 2012, **18,** 12-15.
38 A. Debart, A. J. Paterson, J. Bao, P. G. Bruce, *Angew. Chem. Int. Ed.,* 2008, **47,** 4521-4524.
39 Y. Cui, Z. Wen, Y. Liu, *Energy Environ. Sci.,* 2011, **4,** 4727-4734.
40 J. Suntivich, K. J. May, H. A. Gasteiger, J. B. Goodenough, Y. Shao-Horn, *Science,* 2011, **334,** 1383-1385.
41 J.-L. Shui, N. K. Karan, M. Balasubramanian, S.-Y. Li, D.-J. Liu, *J. Am. Chem. Soc.,* 2012, **134,** 16654-16661.
42 Y.-C. Lu, H. A. Gasteiger, Y. Shao-Horn, *J. Am. Chem. Soc.,* 2011, **133,** 19048-19051.
43 J. Lu, Y. Lei, K. C. Lau, X. Luo, P. Du, J. Wen, R. S. Assary, U. Das, D. J. Miller, J. W. Elam, H. M. Albishri, D. A. EI-Hady, Y.-K. Sun, L. A. Curtiss, K. Amine, *Nat. Commun.,* 2013, **4,** 2383.
44 Y. Lee, J. Suntivich, K. J. May, E. E. Perry, Y. Shao-Horn, *J. Phys. Chem. Lett.,* 2012, **3**, 399-404.
45 Y. Liang, Y. Li, H. Wang, J. Zhou, J. Wang, T. Regier, H. Dai, *Nat. Mater.,* 2011, **10,** 780-786.
46 H. Over, Y. D. Kim, A. P. Seitsonen, S. Wendt, E. Lundgren, M. Schmid, P. Varga, A. Morgante, G. Ertl, *Science,* 2000, **287,** 1474-1476.
47 Y. Inoue, *Energy Environ. Sci.,* 2009, **2,** 364-386.
48 Z. L. Jian, P. Liu, F. J. Li, P. He, X. W. Guo, M. W. Chen, H. Zhou, *Angew. Chem. Int. Ed.,* 2014, **53,** 442-446.
49 E. Yilmaz, C. Yogi, K. Yamanaka, T. Ohta, H. R. Byon, *Nano Lett.,* 2013, **13,** 4679-4684.
50 H.-G. Jung, Y. S. Jeong, J.-B. Park, Y.-K. Sun, B. Scrosati, Y. J. Lee, *ACS Nano,* 2013, **7,** 3532-3539.
51 B. Sun, P. Munroe, G. Wang, *Sci. Rep.,* 2013, **3,** 2247.
52 S. Tabata, H. Iida, T. Horie, S. Yamada, *Med. Chem. Commun.,* 2010, **1,** 136-138.
53 J. Choma, J. Górka, M. Jaroniec, A. Zawislak, *Top Catal.,* 2010, **53,** 283-290.
54 F. Kim, J. Luo, R. Cruz-silva, L. J. Cote, K. Sohn, J. Huang, *Adv. Funct. Mater.,* 2010, **20,** 2867-2873.
55 J. Li, H. Zhang, Y. Zhang, M. Wang, F. Zhang, H. Nie, *Nanoscale,* 2013, **5,** 4647-4651.
56 S. R. Younesi, S. Urbonaite, F. Björefors, K. Edström, *J. Power Sources,* 2011, **196,** 9835-9838.
57 X.-H. Yang, P. He, Y.-Y. Xia, *Electrochem. Commun.,* 2009, **11,** 1127-1130.
58 C.K. Park, S.B. Park, S.Y. Lee, H. Lee, H. Jang, W.L. Cho, *Bull. Korean Chem. Soc.,* 2010, **31,** 3221-3224.
59 V. S. Bryantsev, V. Giorddani, W. Walker, M. Blanco, S. Zecevic, K. Sasaki, J. Uddin, D. Addison, G. V. Chase, *J. Phys. Chem. A,* 2011, **115,** 12399-12409.
60 S. A. Freunberger, Y. Chen, Z. Peng, J. M. Griffin, L. J. Hardwick, F. Bardé, P. Novák, P. G. Bruce, *J. Am. Chem. Soc.,* 2011, **133,** 8040-8047.
61 B. D. McCloskey, D. S. Bethune, R. M. Shelby, G. Girishkumar, A. C. Luntz, *J. Phys. Chem. Lett.,* 2011, **2,** 1161-1166.
62 S. A. Freunberger, Y. Chen, N. E. Drewett, L. J. Hardwick, F. Bardé, P. G. Bruce, *Angew. Chem. Int. Ed.,* 2011, **50,** 8609-8613.
63 K. R. Ryan, L. Trahey, B. J. Ingram, A. K. Burrell, *J. Phys. Chem. C,* 2012, **116,** 19724-19728.
64 J.-J. Xu, D. Xu, Z.-L. Wang, H.-G. Wang, L.-L. Zhang, X.-B. Zhang, *Angew. Chem. Int. Ed.,* 2013, **52,** 3887-3890.
65 C. O. Laoire, S. Mukerjee, K. M. Abraham, E. J. Plichta, M. A. Hendrickson, *J. Phys. Chem. C,* 2010, **114,** 9178-9186.
66 L. Wang, M. Ara, K. Wadumesthrige, S. Salley, K.Y. Simon Ng, *J. Power Sources,* 2013, **234,** 8-15.
67 X. Lin, L. Zhou, T. Huang, A. Yu, *J. Mater. Chem. A,* 2013, **1,** 1239-1245.